Earth and Planetary Science Letters 553 (2021) 116623

Contents lists available at ScienceDirect

Earth and Planetary Science Letters

www.elsevier.com/locate/epsl

Competition between preslip and deviatoric stress modulates precursors for laboratory earthquakes

Srisharan Shreedharan [a,*], David Chas Bolton [a], Jacques Rivière [b], Chris Marone [a,c]

[a] Dept. of Geosciences, Pennsylvania State University, University Park, PA 16802, USA
[b] Dept. of Engineering Science and Mechanics, Pennsylvania State University, University Park, PA 16802, USA
[c] Dipartimento di Scienze della Terra, La Sapienza Università di Roma, Italy

ARTICLE INFO

Article history:
Received 31 July 2020
Received in revised form 30 September 2020
Accepted 1 October 2020
Available online xxxx
Editor: R. Bendick

Keywords:
fault mechanics
earthquake precursors
friction
laboratory earthquakes
elastic waves
stick-slip

ABSTRACT

Variations in elastic wave velocity and amplitude prior to failure have been documented in laboratory experiments as well as in a limited number of crustal earthquakes. These variations have generally been attributed to fault zone healing, changes in crack density, or pore fluid effects modulated dilatation or fault slip. However, the relationships between amplitude and velocity variations during the seismic cycle, and the underlying mechanisms of precursors to failure remain poorly understood. Here, we perform frictional shear experiments and measure the evolution of elastic wave velocity and amplitude throughout the laboratory seismic cycle. We find that elastic amplitudes and velocities undergo clear preseismic variations prior to fault failure. While preseismic amplitude reduction occurs early in the interseismic period, wave speed reduces later, just prior to failure. We perform a complementary set of stress oscillation experiments to quantify the response of seismic amplitudes and velocities to variations in the stress tensor. Taken together, our results indicate that preseismic amplitude variations are primarily controlled by fault slip rate and acceleration. On the other hand, elastic velocity responds to a combination of fault preslip which reduces seismic wavespeed and increasing stress in the wallrock, which increases wavespeed. Our data show that precursory changes in seismic wave speed may be more common than previously thought because they are masked by changes in wallrock stress. These results underscore the importance of continuous and long-term time-lapse monitoring of crustal faults for seismic hazard assessment and potential precursors to failure.

1. Introduction

Earthquakes are intensely destructive and, thus, earthquake prediction and forecasting has attracted much interest among seismologists for many years (Milne, 1880; Scholz et al., 1973). Broadly, earthquake prediction research has focused on time and/or slip predictable models of earthquake recurrence intervals (e.g. Shimazaki and Nakata, 1980) or searches for precursory evidence that could point to the eventual timing or size of earthquakes (e.g. Scholz et al., 1973). However, most studies found either a lack of robust precursors or significant variations in recurrence intervals (e.g., Geller, 1997). For instance, the Parkfield Earthquake Prediction Experiment (Bakun et al., 2005) was designed from observations of five M6 earthquake sequences in the Parkfield segment of the San Andreas fault prior to 1985. Based on the recurrence time and event history seismologists expected a sixth event to occur before 1993; and they instrumented the region to study preslip and pre-nucleation processes. However, the event eventually occurred in September 2004 and lacked any measurable precursor despite an array of instruments.

Reliable field observations of earthquake precursors have proven difficult (Main et al., 2012; Pritchard et al., 2020). However, laboratory experiments designed to study brittle fracturing (Brace et al., 1966), granular failure (Kaproth and Marone, 2013) and shear failure (Sammonds et al., 1992) have routinely documented preseismic signatures preceding macroscopic failure. These take the form of pre-failure dilatancy, anomalies in elastic wave properties or interseismic variations in the Gutenberg-Richter b-value etc. among a variety of other precursory phenomena (see Cicerone et al., 2009 for a review). Recent advances in high resolution cross-borehole active seismic instrumentation have helped document precursory seismic velocity reduction prior to a M_w 3 earthquake (Niu et al., 2008). Similarly, Malagnini et al. (2019) utilize repeating earthquakes to observe an approximately 12-month long preseismic attenuation variation prior to the 2003 M_w 6.5 San Simeon earthquake, which they attribute to fluctuations in near-fault crack

* Corresponding author.
E-mail address: srisharan@psu.edu (S. Shreedharan).

https://doi.org/10.1016/j.epsl.2020.116623

density. However, an ambient noise interferometry study by Brenguier et al. (2008) documented no similar preseismic wave velocity variation. A lack of preseismic velocity anomalies in this latter study could represent a real absence of precursory activity or it may simply be that ambient noise tomography is unable to resolve variations (e.g. of crack densities) at depth. In another example, Chiarabba et al. (2020) performed seismic tomography for the fault zone participating in the 2016 Mw 6.5 Norcia earthquake. They documented an increase in P-wave velocity on the primary locked patch lasting for ∼2 months and a local P-wave velocity reduction near the hypocenter for a few weeks before the mainshock. There is a clear need to improve our understanding of laboratory-based observations of precursors and to test process-based models using field observations.

Over the past ∼50 yrs, significant advances have been made in quantifying the velocity and attenuation response of elastic waves during the brittle deformation and subsequent failure of dry and saturated porous rocks (e.g. Stanchits et al., 2003). It is now widely accepted that significant variations in elastic velocities and attenuation precede brittle failure of rocks due to variations in crack densities and saturation state of pore spaces (see sections 5.4 of Paterson and Wong, 2005 and references therein). Additionally, observations of seismic wave velocities in laboratory frictional sliding experiments have shown robust preseismic P-wave velocity reductions during the preparatory stages prior to fault failure (Kaproth and Marone, 2013; Scuderi et al., 2016; Hedayat et al., 2018). These variations have been attributed to fault zone dilation, variations in porosity/crack densities and fault zone preslip. Similarly, precursory P-wave amplitude variations during laboratory stick-slip instabilities have been attributed to preslip (Hedayat et al., 2014; Shreedharan et al., 2020), with larger and earlier precursors for larger seismic events (Passelègue et al., 2017; Acosta et al., 2019; Shreedharan et al., 2020). Despite these advances in fault zone monitoring in the lab and in nature, the relationship between amplitude and velocity variations, and the precise mechanisms responsible for these variations, particularly in the context of frictional sliding, are not well constrained. Additionally, the question of how these reproducible laboratory precursors scale to crustal faults remains unanswered.

Here, we present a detailed analysis of the evolution of fault zone elastic properties prior to an extensive set of laboratory earthquakes. We describe frictional sliding experiments on granite surfaces instrumented with continuous active ultrasonic monitoring (Kaproth and Marone, 2013; Shreedharan et al., 2019, 2020). We analyze the temporal evolution of P-wave amplitudes and velocities and find that precursory amplitude variations begin early in the seismic cycle and well before velocity reduction, which occurs just prior to failure. We complement our measurements with Dynamic Acoustoelastic Testing (DAET), an experimental protocol used to track the nonlinear elastic response of materials (Rivière et al., 2013). Our data indicate that preseismic velocity changes arise from both fault creep and changes in stresses in the wall-rock. Significantly, changes in wave amplitude precede changes in wave speed in a robust fashion that can be tied to the competing effects of fault creep and deviatoric stress on seismic wave speed. This experimental investigation represents a novel joint analysis of preseismic amplitude and velocity response using a combination of nonlinear elastic testing and friction experiments, to pinpoint the precise mechanisms responsible for preseismic anomalies. Our experiments demonstrate the feasibility of time-lapse fault zone monitoring as a tool to identify precursors to lab earthquakes. Taken together with notable examples of preseismic anomalies in nature, we suggest that this may also be true for crustal seismicity.

2. Methods

2.1. Friction experiments

The friction experiments reported here were performed in a double-direct shear (DDS) configuration in a biaxial testing apparatus in the Penn State Rock Mechanics laboratory. In this configuration, three rock blocks are sandwiched together to form two fault interfaces and the longer central block is loaded to shear the two fault interfaces (Fig. 1a). Our experiments were performed on samples with a nominal frictional contact area of 5 x 5 cm^2. Experimental reproducibility was ensured by performing an extensive set of tests, including repeats at a given set of conditions, at room temperature and controlled relative humidity of 100% (Table 1).

The biaxial apparatus is fully servo-controlled with a horizontal and vertical hydraulic piston applying the normal and shear forces respectively. Shear and horizontal forces were recorded using calibrated strain gauge load cells accurate to ±5 N. Horizontal (normal) and vertical (shear) load point displacements were recorded using direct current differential transformers (DCDTs). Additionally, a DCDT attached to the central shearing block, referenced to the base of the DDS configuration was used to measure fault slip. All DCDTs have a displacement resolution of ±0.1 μm and were calibrated using a Vernier height gauge. All mechanical data were acquired at 10 kHz with a 24-bit ±10 V analog-to-digital converter and averaged in real-time to 100-1000 Hz.

Following Shreedharan et al. (2020), we sheared rough Westerly granite surfaces decorated with a thin dusting of quartz power (∼0.25 g by mass and ∼250 μm layer thickness prior to normal load application) to simulate frictional wear material. The granite surfaces were surface ground flat and roughened with #60 grit silicon carbide to produce an RMS roughness of ∼20 μm. The compacted gouge layers, after application of normal stress and shear, were comparable in thickness to the roughness of the granite interfaces. This ensured that frictional contact involved a combination of direct interaction between the granite surfaces and contact within the wear material and between the solid granite and wear material (see supplementary Fig. S1). All experiments reported in this study were performed at a nominal normal stress of 10 MPa and a shear rate of 11 μm/s. We generated the spectrum of slip modes, from slow to fast, by using a range of spring stiffnesses in series with the shear load point, following the approach of Shreedharan et al. (2020). We varied elastic stiffness by constructing acrylic blocks of varying cross-sectional area (see Fig. 1 of Shreedharan et al., 2020), which allowed us to produce the full spectrum of slip modes from fast to slow (e.g., Leeman et al., 2016).

2.2. Ultrasonic monitoring of shear experiments

In addition to mechanical data acquisition, all experiments were instrumented with an ultrasonic acoustic monitoring system. Active ultrasonic pulses were transmitted through the experimental faults using broadband (∼0.02 – 2 MHz) lead-zirconate (PZT) P-polarized ultrasonic transducers (Boston Piezo-Optics Inc. PZT-5A 0.5″ diameter compression crystals) with a resonant frequency of 500 kHz. The transducers were epoxied at the bottom of blind holes in steel loading platens and the platens were then coupled to the DDS configuration using molasses (Fig. 1a). The sensors were activated by a half-sinusoidal 500 kHz, 28 V source function every 1 ms and the received signals were sampled at 25 MHz (2048 samples per waveform). A typical waveform recorded by the receiver PZT is shown in inset to Fig. 1a. The dashed vertical line shows the pulse arrival time which is used to estimate compressional (P-) wave velocity. Here, we use the largest peak-to-peak amplitude within the first 5 μs of the ultrasonic pulse (red wavelet

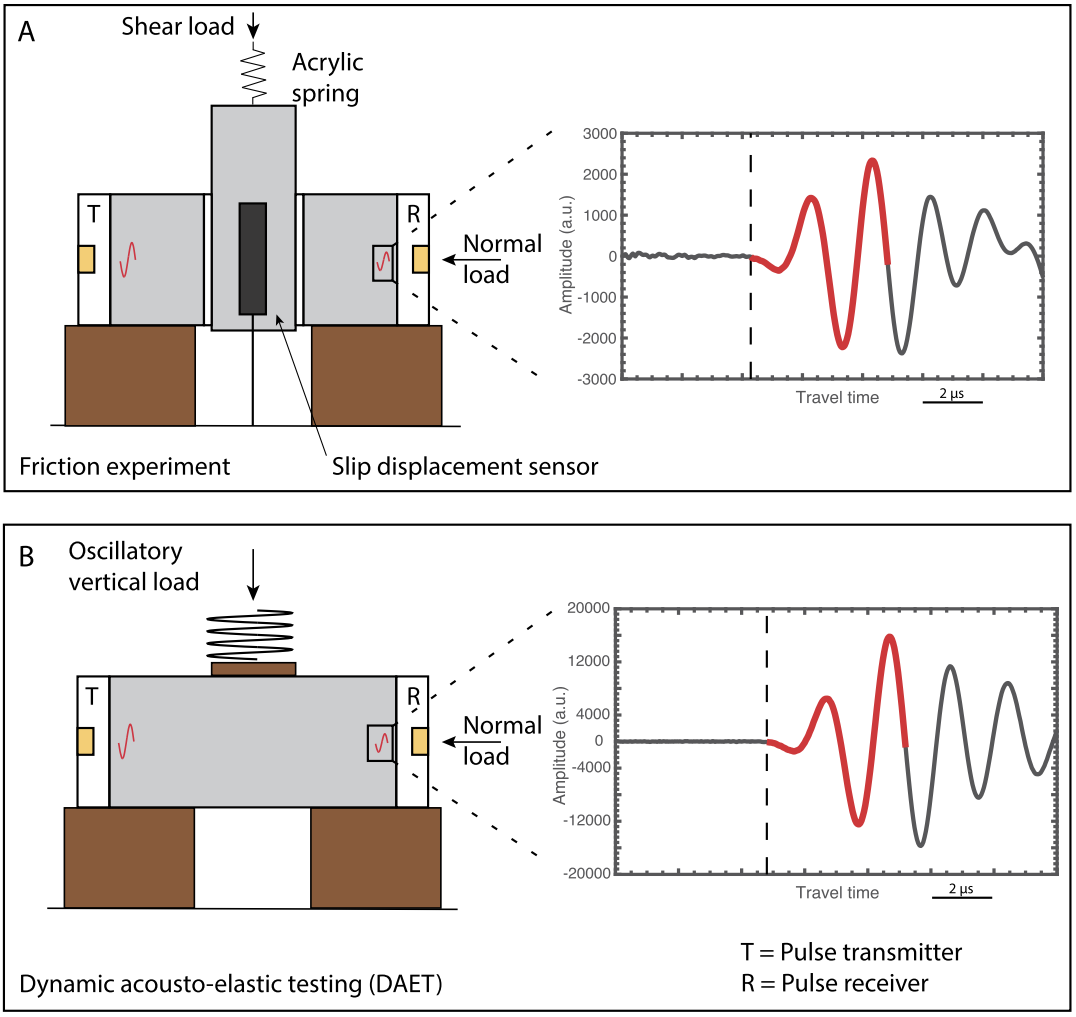

Fig. 1. Experiment configuration and example elastic waves (a) Double-Direct Shear (DDS) friction arrangement with Westerly granite blocks loaded by platens that contain PZTs (gold rectangles) to generate and record elastic waves. The three-block configuration includes two rough surfaces coated with a dusting of fine quartz powder (b) Dynamic Acoustoelastic testing (DAET) procedure using an intact granite block of the same length and boundary conditions as the DDS setup. Insets to both figures show typical ultrasonic pulse. Dashed line shows the P-wave arrival and the red section marks the wavelet used for cross-correlation and amplitude analyses. (For interpretation of the colors in the figure(s), the reader is referred to the web version of this article.)

Table 1
List of experiments and associated boundary conditions reported in this study.

Experiment name	Experiment type	Normal stress (MPa)	Loading velocity (µm/s)	Spring cross-sectional area (cm^2)	Gouge type
p5209	DDS	13	11	25	No dusting
p5221	DDS	13	11	25	Quartz
p5268	DDS	10	1-121	16	Quartz
p5269	DDS	10	1-121	9	Quartz
p5270	DDS	10	1-121	25	Quartz
p5271	DDS	10	1-121	20.25	Quartz
p5272	DDS	10	1-121	12.25	Quartz
p5341	DAET	10	Not applicable	Not applicable	Not applicable
p5344	DAET	10	Not applicable	Not applicable	Not applicable
P5345	DAET	10	Not applicable	Not applicable	Not applicable

DDS = Double Direct Shear Experiment DAET = Dynamic Acoustoelastic Testing.

in inset to Fig. 1a) for ultrasonic analyses, which corresponds to the first arrival rather than the P-wave coda (Shreedharan et al., 2020).

Following previous ultrasonic studies of experimental faults (Nagata et al., 2008; Kilgore et al., 2017), we report the transmitted amplitudes as acoustic transmissivity, |T|. Acoustic transmissivity is defined as the ratio of wave amplitude through the DDS configuration (A_{DDS}) to the amplitude of an equivalent wavelet through an intact block (A_{intact}) of the same material and length dimension:

$$|T| = \sqrt{\frac{A_{DDS}}{A_{intact}}} \quad (1)$$

Here, the square root term accounts for the fact that the ultrasonic pulse travels through two faults (Nagata et al., 2008; Shreed-

haran et al., 2019). We perform this transformation to ensure that we compare the effect of a single fault when discussing variations in ultrasonic amplitudes relative to changes in friction/shear stress and slip/slip rate, which are reported for a single fault.

2.3. Dynamic acoustoelastic testing

Dynamic acoustoelastic testing (DAET) is a nondestructive testing method used to constrain elastic nonlinearity associated with microscopic flaws and other factors (Rivière et al., 2013). Here, the elastic material is subjected to small oscillatory stress or strain perturbations (also referred to as the 'pump') and the response of high-frequency ultrasonic pulses (the 'probe') in a perpendicular direction is measured. Measurements of P-wave velocity and |T| in our frictional shear experiments represent the composite response of the faults and the wallrock surrounding them. Here, we use DAET to quantify the response of P-wave velocity and |T|, with particular focus on changes associated with variations in elastic moduli of the bulk rock outside the fault zone. Subsequently, we remove the effects of bulk/wallrock on our ultrasonic parameters (P-wave velocity and |T|) to isolate the fault response.

We performed DAET-type experiments on an intact block of Westerly granite block that has the same length as the three-block DDS configuration (Fig. 1b). The sample was cut from the same block as our Westerly granite friction samples and subjected to the same normal stress used in our friction experiments (10 MPa). The vertical stress was selected such that the final mean stress and stress state were equivalent to those experienced by the DDS friction configuration. Subsequently, the stress state experienced by the DDS configuration during stick-slip instabilities was simulated in the DAET configuration by subjecting it to deviatoric stress oscillations. The deviatoric stress oscillation amplitudes were similar to the size of stress drops in the friction experiments (shear stress changes of ∼0.3 – 1 MPa). Similarly, we used oscillation frequencies of 0.1 – 1 Hz to simulate the interseismic and co-seismic durations of stick-slips in the friction experiments. Keeping the oscillatory vertical load frequency low also ensures that the generated stress field variations are essentially static in relation to the travel time of the ultrasonic probe (of order ∼10 μs). Overall, we ensure that the single-block DAET configuration was subjected to the same static and dynamic stress-state as the friction experiments. We further characterize quantitatively the distribution of the stress state developed during the DAET experiments by performing a Finite Element Modeling (FEM) simulation (Supplementary Text T1 and Fig. S2). Our models indicate that the vertical load oscillations are mostly accommodated around the middle of the intact block volume in the DAET experiments. This is consistent with the stress state of the DDS geometry where the shear traction is accommodated by the frictional interfaces and wallrock surrounding them. Ultrasonic pulses (probe) were transmitted through the sample and recorded the same as in our friction experiments, and thus along the same path as waves that passed normal to the fault plane (Fig. 1b). A typical P-wave pulse for the DAET test (Fig. 1b) shows a significantly larger peak-to-peak amplitude compared to the peak-to-peak amplitude of the DDS configuration (Fig. 1a); as expected because the wave travels through intact rock and does not traverse the fault planes. Supplementary Fig. S3 shows a side-by-side comparison of the three-block DDS configuration and the single-block DAET configuration for reference.

2.4. Compressional wave velocity estimation

To estimate the P-wave velocity in our ultrasonic experiments, we first estimate precise delay times by cross-correlating waveforms against a 'master' waveform for all pulses in each stick-slip instability (e.g. Kaproth and Marone, 2013; Scuderi et al., 2016). The arrival time for the master waveform is handpicked and the underlying errors are typically less than 0.1 μs (Kenigsberg et al., 2019). After the cross-correlation procedure, we retain only pulses with correlation coefficient >0.98 for subsequent analyses. We further estimate delay times to sub-sample precision by utilizing a parabolic curve-fitting procedure (e.g., Céspedes et al., 1995; Niu et al., 2008). Here, we fit a parabola to the three largest samples of the cross-correlation function. The peak of this continuous parabolic function determines the delay-time to sub-sample precision.

However, because the arrival times include the time spent by the pulse in the steel PZT blocks (Fig. 1), we estimate a travel time correction factor (e.g., Scuderi et al., 2016). This is accomplished with a simple calibration exercise where travel times are estimated for ultrasonic pulses passing through westerly granite blocks of different thicknesses. A plot of block thickness versus travel time is a straight line with slope corresponding to a composite velocity through the granite block and steel. The y-intercept, or zero-thickness travel time intercept (t_0) is the time spent by the ultrasonic pulse in the steel platens (Supplementary Fig. S4). Then, knowing the thickness of the DDS setup or the DAET setup (D), and the total travel time (t) through these setups, the precise P-wave velocity, v_p, can be calculated as

$$v_p = \frac{D}{t - t_0} \tag{2}$$

3. Results

3.1. Friction experiments with ultrasonic monitoring

We studied the evolution of ultrasonic v_p and |T| during stick-slip instabilities, as described above. We modified the effective shear loading stiffness to modulate the fault slip behavior (e.g., Leeman et al., 2016) while ensuring that the real contact area remained the same between experiments (Shreedharan et al., 2020). A plot of shear stress evolution as a function of loadpoint displacement for a typical friction experiment is shown in Fig. 2.

Each experiment began with load-unload-reload cycles prior to 5 mm of cumulative slip to estimate loading stiffness (Shreedharan et al., 2019) and promote shear localization (Frye and Marone, 2002). We sheared the experimental faults to a cumulative total slip of ∼30 mm. We observed the onset of quasi-dynamic instabilities at ∼5-7 mm of load point displacement after which shear transitioned into quasi-periodic stick-slip or slow slip instabilities depending on the stiffness of the acrylic spring used.

The inset to Fig. 2 shows a sequence of stick-slip instabilities and their associated ultrasonic/seismic attributes. The vertical arrows denote the peak of shear stress, v_p, and |T| for a laboratory earthquake. While the fault attains its peak shear strength just prior to failure, the peak in |T| occurs significantly earlier in the interseismic period. Shreedharan et al. (2020) demonstrated that the increase in |T| following co-seismic failure is due to fault healing (an increase in real area of contact at the frictional interface) and the reduction in |T| is caused by fault preslip (which destroys contact area via shear). It is interesting to note, however, that the v_p does not follow the trends in |T|. Instead v_p consistently increases during the interseismic period and reduces slowly just prior to failure, followed by rapid reduction during the coseismic phase. Previous studies have documented such precursory variations in v_p (e.g. Kaproth and Marone, 2013; Scuderi et al., 2016) and attributed it to preslip and dilation. However, existing works do not consider the connections between transmitted amplitudes and wave speed for frictional sliding, nor do they document the temporal evolution during the seismic cycle for multiple stick-slip

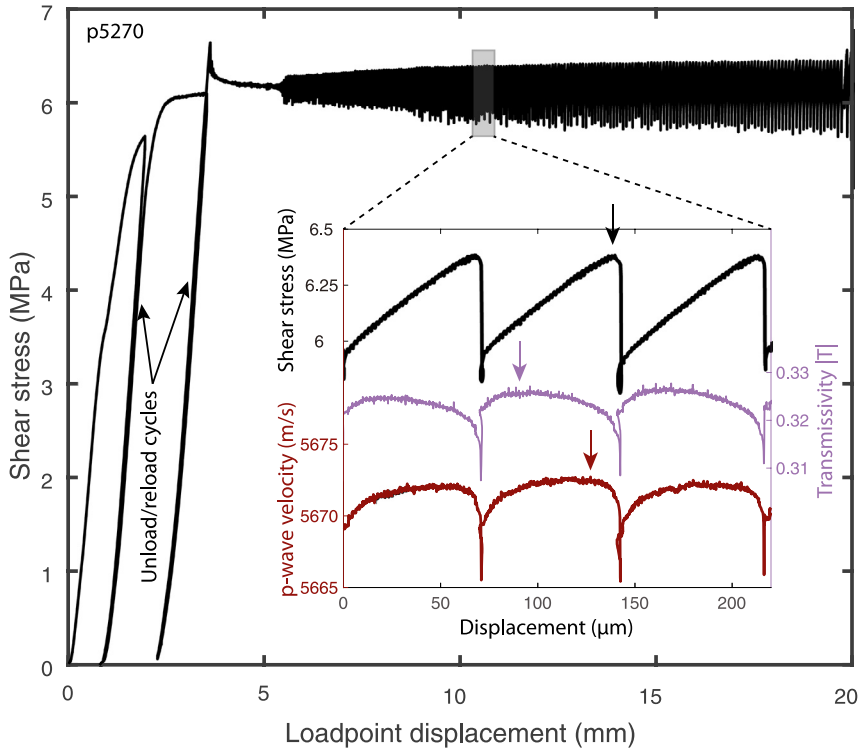

Fig. 2. Data for one complete frictional shear experiment showing evolution of shear stress as a function of shear loadpoint displacement. Quasi-dynamic slow slip instabilities begin at ~5 mm of shear and evolve into fully dynamic fast stick-slip instabilities. Inset shows shear stress and ultrasonic data for three lab seismic cycles with arrows showing the onset of shear failure (black), |T| reduction (purple) and V_p reduction (brown). Note that |T| and V_p increase during the initial phase of load increase and that |T| reaches a peak well before the peak in V_p prior to failure.

and slow slip events. Here, we quantify the evolution of |T| and v_p and demonstrate that this difference in evolution behavior can be explained by carefully considering the effect of the stress state on |T| and v_p.

3.2. Dynamic acoustoelastic testing

The evolution of acoustic transmissivity and wave velocity during the laboratory seismic cycle document fault zone and wallrock processes. During the interseismic period of loading, deviatoric stress increases and fault creep begins. Simultaneously, microcracks in the wallrock surrounding the fault experiences an increase in mean and deviatoric stress because fault zone shear stress increases at constant normal stress. The stress state and fault slip are highly coupled throughout the pre-seismic phase of the seismic cycle. To decouple the effects of stress and fault slip on variations in |T| and v_p, we performed a series of DAET experiments and used the calibrations described above (Fig. 3). We focus here on nonlinear elastic processes within the wallrock surrounding the fault.

In DAET experiments we subjected an intact block of Westerly granite (see Supplementary Fig. S2) to the same background stress state (Fig. 1) as experienced by the DDS configuration. Then, we simulated the stress variations during stick-slip instabilities by performing vertical stress oscillations at 0.1 – 1 Hz to encompass the range of frequencies representative of the lower frequency interseismic and higher frequency coseismic period. The P-wave amplitude and velocity response to these stress oscillations is shown in Fig. 3a-c for 0.1, 0.3 and 1 Hz. Generally, we observe that while the v_p response strongly follows the stress oscillations, the amplitude response is less dependent on the stress variations (also see Supplementary text T1 and Fig. S2).

We quantify the stress dependence of |T| as the slope of the cross-plot between the P-wave amplitude and the vertical stress perturbation, and denote this parameter as β_a (Fig. 3d). We similarly define the stress dependence of v_p and denote it as β_v (Fig. 3e). These β parameters represent the amount of quadratic nonlinearity in Westerly granite (β_v itself is related to the third-order elastic constants) and are often used to estimate the amount of 'microdamage' in materials (Rivière et al., 2013). Nonlinearity in rocks (i.e., β) generally decreases with increasing effective stress, as micro-cracks and grain-grain contacts close (Rivière et al., 2016). Given the amount of scatter in the data (Fig. 3d-e), we cannot properly resolve higher-order nonlinear effects, and we therefore assume that quadratic nonlinear effects (i.e., β) dominate the response. As seen in Fig. 3d-e, we do not observe systematic variations in β_a or β_v in response to different stress oscillation frequencies, which is consistent with previous observations in intact Berea sandstone (Rivière et al., 2016). Hence, we use averaged values of 21.89 and 5.76 for β_a and β_v respectively for subsequent analyses. We note here that while the nonlinear parameters are most often expressed as a relationship between elastic wavespeed (or elastic modulus) and *strain* in a sample, we express it as a relationship between wavespeeds and stress (Rivière et al., 2016), as the latter represents our controlling variable.

4. Discussion

4.1. Role of wallrock stress on v_p and |T|

Our DAET analysis (Fig. 3) indicates that the fault zone wallrock plays an important role in the evolution of |T| and v_p during the lab seismic cycle. In particular, for small stress perturbations relative to the background stress state, approximately 6 m/s of the variation in v_p per 1 MPa change in stress can be explained by variations in stress in the wallrock during interseismic loading (Fig. 3e). The magnitude of this change is comparable to the amount of v_p variation shown during the inter- and pre-seismic portion of stick-slips in DDS experiments (Inset to Fig. 2). This

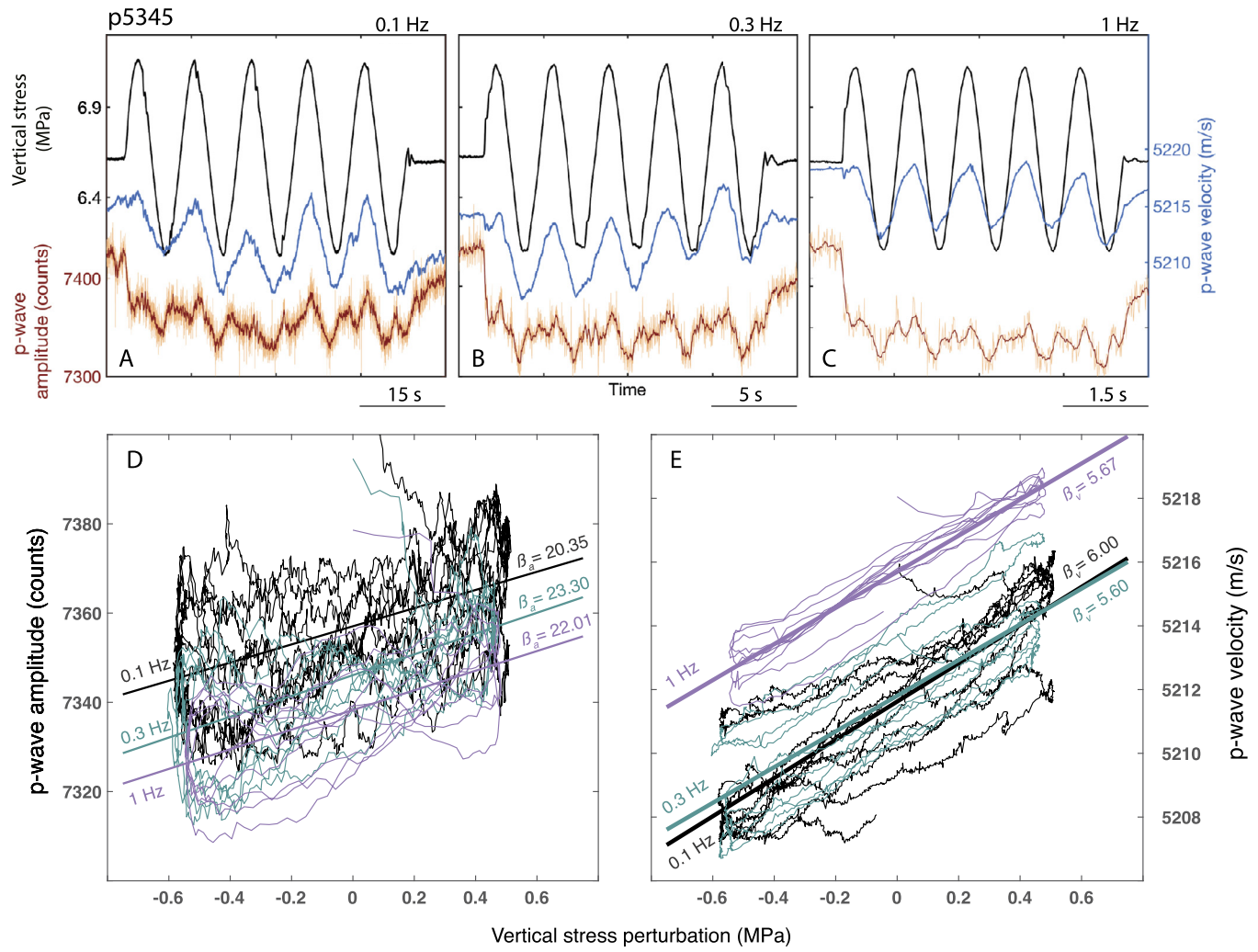

Fig. 3. (a)-(c) DAET test results for 1 MPa amplitude oscillations of the vertical stress (see Fig. 1b) at frequencies of (a) 0.1 Hz (b) 0.3 Hz and (c) 1 Hz. Note that the P-wave velocity (blue) tracks stress oscillations with negligible phase lag whereas P-wave amplitude (orange - raw amplitudes, red - moving mean of amplitude) variations have significantly lower signal to noise ratio. (d) Cross-plots of amplitude and stress for the data show in (a)-(c). The lines show best fit linear relationships for each frequency. (e) Cross-plot of velocity and stress for the data show in (a)-(c) for all test frequencies. The lines show best fit linear relationships for each frequency.

raises the possibility that a significant fraction of the pre- and post-seismic variations in v_p observed during laboratory stick-slip instabilities could be attributed to stress-modulated effects rather than fault zone processes. Here, we isolate the effect of wallrock stress on |T| and v_p using data acquired from the DAET experiments.

Given that the wavelength of the ultrasonic pulses used here (a few millimeters) is significantly larger than the width of each fault interface (< 0.2 mm), the faults are treated as displacement discontinuities (Pyrak-Nolte et al., 1990) rather than an actual medium or 'zone'. We denote the velocity of the pulse passing through our DDS configuration (Inset to Fig. 2) as v_{DDS}. Then, v_{DDS} is a stress and fault slip dependent P-wave velocity which can be represented at a given stress state as

$$v_{DDS} = v_{slip} + \Delta v_\sigma \tag{3}$$

Here, v_{slip} represents the wave velocity corrected from stress changes in the wallrock and, as we shall see, it appears to be primarily controlled by fault slip. The parameter Δv_σ accounts for velocity changes due to wallrock stress perturbations during stick-slips. Note that because the normal stress in our experiments is constant, we attribute P-wave velocity variations across the fault entirely to fault slip. In instances where it is important to consider time varying normal stress, it may be necessary to consider its additional effect on the velocity (Pyrak-Nolte et al., 1990).

Using the velocity-stress relationships determined from DAET measurements in Fig. 3e, Eq. (3) can be rewritten as

$$v_{slip} = v_{DDS} - \beta_v \Delta\sigma \tag{4}$$

Where we have used $\Delta v_\sigma = \beta_v \Delta\sigma$, and where $\Delta\sigma$ represents the variation in stress state (within the wallrock of the DDS configuration) during the stick-slip instabilities. As far as the amplitude is concerned, both ultrasonic amplitudes A_{intact} and A_{DDS} in Eq. (1) depend on stress perturbations arising due to stick-slip instabilities. Then, Eq. (1) can be rewritten, accounting for this effect, as

$$|T|_{slip} = \sqrt{\frac{A_{DDS} - \beta_a \Delta\sigma}{A_{Intact} - \beta_a \Delta\sigma}} \tag{5}$$

We demonstrate the effect of wallrock stress variations on |T| and v_p in Fig. 4. Fig. 4a shows the shear stress evolution for a single stick-slip instability in the DDS configuration. Following Shreedharan et al. (2020), we separate this shear stress curve into three portions. First, the interseismic period is identified from the linear-elastic portion of the curve, where load increases in proportion to the shear load stiffness. In this period, the fault is effectively locked

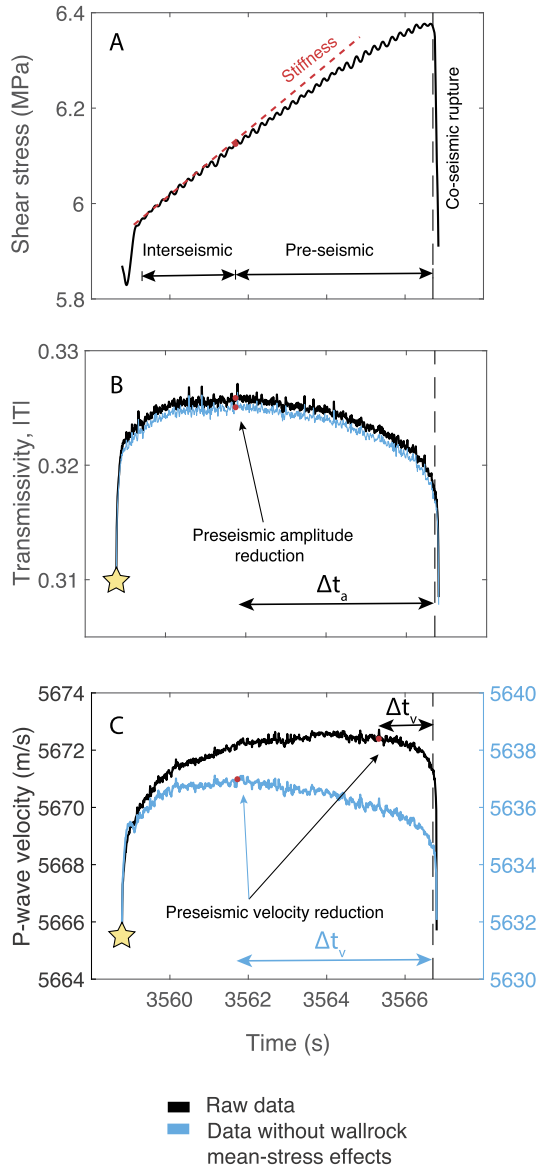

Fig. 4. Detail of three phases of the lab seismic cycle defined by (a) shear stress evolution for a typical labquake. Interseismic period is the linear-elastic portion of the load-up curve. Preseismic creep begins at the onset of nonlinear loading and ends at the peak stress. (b) Acoustic wave transmissivity |T| showing raw data for waves passing through the fault zone and data correcting for stress state. Stress effects on |T| are observable but small. (c) Raw data for velocity of P-waves passing through the fault zone and data correcting for stress state. Note that raw P-wave velocity continues to increase well into the preseismic portion of the seismic cycle; however, data corrected for stress peaks and begins to decrease at the onset of fault creep consistent with |T| evolution. Yellow star indicates the location of master ultrasonic waveform used for cross-correlation.

and experiences a slip rate far below the background loading rate. Second, the preseismic phase of the shear loading curve is marked by a deviation from elastic loading. This marks the onset of preseismic slip and this phase ends at the peak value of shear stress. The final phase of shear stress evolution is the coseismic phase. Here, the fault experiences a stress drop, and fault slip rate accelerates to a coseismic maximum.

We observe that |T| is markedly sensitive to these slip rate modulated variations in shear stress (Fig. 4b). In other words, |T| increases throughout the linear-elastic phase and reaches a maximum at the onset of preslip. Once the fault unlocks |T| decreases continuously until co-seismic failure. This is consistent with previous observations by Hedayat et al. (2014) and Shreedharan et al. (2020) where fault zone preslip was found to be the primary control on ultrasonic amplitude evolution during shear stress variations. Interestingly, we find that the role of stress variations on |T| is minimal and correcting for it (Fig. 4b – blue curve) is inconsequential to our interpretations. This further validates the idea that |T| and attenuation in natural faults (e.g. Malagnini et al., 2019) may be very sensitive to small preseismic variations in fault zone slip rate.

In stark contrast to the evolution of |T| during the laboratory seismic cycle, we find that the composite v_p (or v_{DDS}) evolves in a complex manner (Fig. 4c – black curve). The raw P-wave velocity increases consistently during the interseismic and well into the preseismic period, reducing just prior to macroscopic failure. However, if one accounts for the role of wallrock stress state there is a much larger reduction in v_p, and the changes begin earlier in the seismic cycle (blue curve in Fig. 4c). The P-wave velocity variation due to fault slip alone, v_{slip}, qualitatively resembles |T| and attains a peak value at the transition from linear-elastic loading to inelastic fault slip.

Variations in the wallrock stress state have an important impact on the evolution of elastic wave speed during the seismic cycle. These nonlinear elastic effects in the wallrock mask and significantly delay the elastic wave speed precursor. Our measurements show that such changes impact v_p much more so than |T|. This variation in v_p is comparable in size and opposite in sign to the role of preslip on modulating v_p and |T|. The competition between these effects in the preseismic period could modulate the size and timing of precursory observations of v_p and |T| in the lab and in nature.

We further validate this observation by quantifying the timing of onset of the precursor prior to fault failure as Δt_a and Δt_v for the |T| and v_p precursors respectively (Fig. 4b-c). We estimate Δt_a and Δt_v using the raw ultrasonic data and data corrected for the effect of wallrock stress variations. We report a cross-plot of the Δt_a and Δt_v precursor timings along with a 1:1 line for comparison in Fig. 5. The size of these precursory signatures is directly related to the stick-slip recurrence intervals. In other words, lab earthquakes with larger recurrence interval have longer precursor duration. For the raw ultrasonic attributes, the onset of the preseismic |T| reduction occurs up to 50% earlier in the seismic cycle. However, this trend disappears after accounting for the v_p modulation due to shear stress variations in the wallrock and the precursory variations in |T| and v_p due to preseismic slip alone follow the 1:1 line well. This difference between |T| and v_p behaviors becomes insignificant for smaller labquakes, and the raw and corrected datasets collapse for precursor durations of less than 2 s.

Previous observations of precursory v_p variations in the lab by Kaproth and Marone (2013) and Scuderi et al. (2016) were made in layers of sheared fault gouge. In these experiments, fault zone fabric evolves to produce narrow zones of localized slip flanked by wider 'spectator' regions (Scuderi et al., 2017) which participate minimally (or not at all) in fault slip. In such cases, in the absence of intact wallrock, it is unclear what the role of shear stress would be in modulating the observed precursors. However, since compacted and sheared granular media have different elastic moduli and wavespeeds (e.g. Knuth et al., 2013; Kenigsberg et al., 2019), we posit that spectator regions may act as wallrock and significantly contribute to the v_p variations occurring due to shear stress perturbations. Additionally, the presence of fluids in the pore spaces (saturation) of the wallrock and fault zone may further enhance or mask (depending on fault zone hydrologic properties and survey location) such variations in v_p and attenuation (Stanchits et al., 2003; Paterson and Wong, 2005). Faults in nature where wavespeed variations have been observed preseismically (Niu et al., 2008) and post-seismically (Brenguier et al., 2008; Pei et al., 2019) have complex structures including multiple off-fault strands

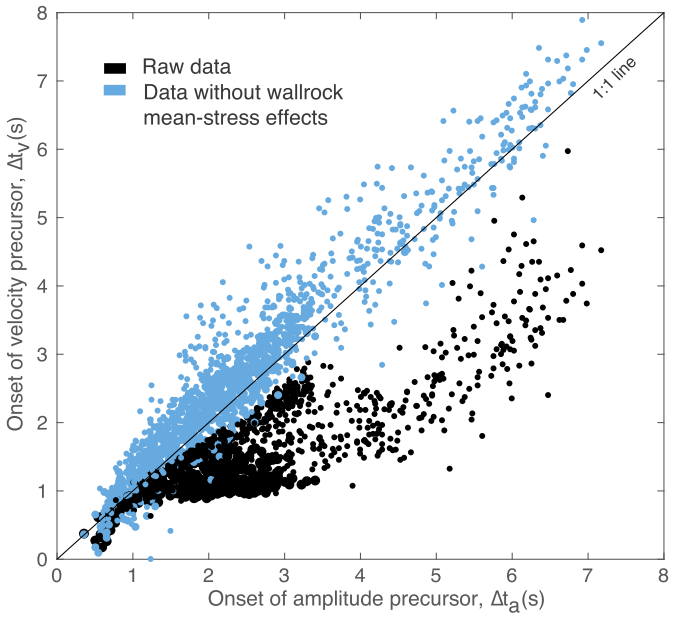

Fig. 5. Comparison of precursor durations derived from v_p and |T| (see Fig. 4). Solid line shows 1:1 correlation. Raw data are in black and data corrected based on the DAET experiments are in blue. Raw data show that the amplitude precursor (Δt_a) is significantly longer than the velocity precursor Δt_v while the DAET-corrected data fall approximately on to the 1:1 line, indicating that both elastic wave amplitude and velocity begin to decrease when fault creep begins.

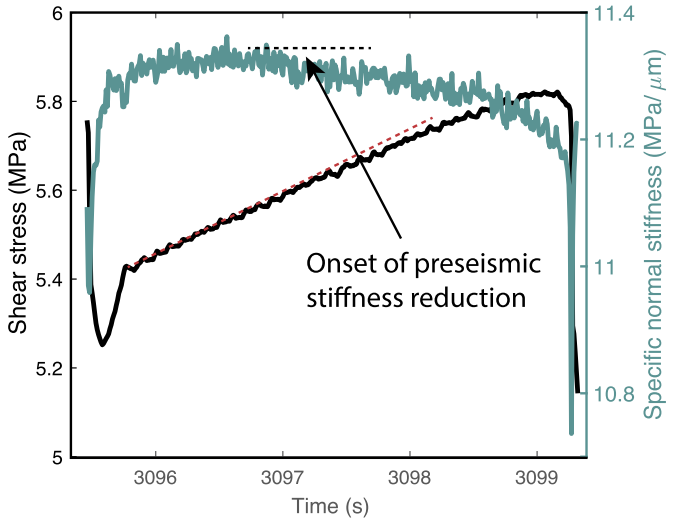

Fig. 6. Evolution of fault specific normal stiffness (green) and shear stress (black) during a typical lab seismic cycle. Fault contact stiffness increases rapidly initially during the linear-elastic (red dashed line) interseismic healing phase and begins to reduce at the onset of preseismic slip.

and damage zones (e.g. Savage and Brodsky, 2011; Passelègue et al., 2016). Numerous studies show that elastic nonlinearity is highly sensitive to the presence of micro-damage and imperfect cementation between grains (e.g., Adams and Williamson, 1923). Here, our study shows that these nonlinear elastic effects are significant in host rock made of intact granite blocks, therefore we expect an even more pronounced influence in nature when off-fault damage is present in the wallrock (e.g. Aben et al., 2019).

4.2. Evolution of specific stiffness during stick-slip instabilities

Ultrasonic attributes such as |T| and v_p are particularly useful for studying the evolution of microscopic elastic and plastic asperity deformation during frictional shear (Pyrak-Nolte et al., 1990; Nagata et al., 2008; Hedayat et al., 2014; Kilgore et al., 2017; Shreedharan et al., 2019). This is because |T| is linearly related to contact diameter and contact specific stiffness (Kendall and Tabor, 1971). Following Kilgore et al. (2017), for a displacement discontinuity (i.e., when the fault zone width is significantly smaller than the probe wavelength), the specific normal stiffness, k_{sp}, for the interface can be expressed as a function of the angular frequency of the pulse, ω, the density of the surrounding medium, ρ (we calculated $\rho = 2630$ kg/m^3 for our Westerly granite blocks), the P-wave velocity of the pulse through intact granite, v_p, and the transmissivity, |T| as

$$k_{sp} = \frac{\omega \rho v_p}{2\sqrt{\frac{1}{|T|^2} - 1}} \tag{6}$$

Note that |T| and v_p both evolve during the laboratory seismic cycle in our experiments. While the evolution of |T| is primarily modulated by fault zone preslip, v_p is modulated by a combination of opposing effects from preslip of the fault and increased stress in the wallrock.

Using Eq. (6), we estimate the evolution of k_{sp} for our laboratory instabilities (Fig. 6). The fault zone specific normal stiffness is remarkably similar to the |T| evolution (see Fig. 4b) and the effect of changes in v_p on k_{sp} is minimal. Additionally, k_{sp} shows a modest preseismic, precursory reduction of ~100 kPa/μm (~1%), and a coseismic reduction of ~ 400 kPa/μm (~4%). Observations of preseismic phenomena such as preslip in faults in nature remain scarce (e.g., Amoruso and Crescentini, 2012). However, the few well-documented observations of preslip prior to large earthquakes such as the 2001 Mw 8.4 Peru earthquake (Melbourne and Webb, 2002) and the 2011 Tohoku-Oki earthquake (Uchida and Matsuzawa, 2013) record preseismic slip of 2 – 20 cm. Because specific stiffness and |T| variations are empirically proportional to the logarithm of the fault slip rate rather than the absolute amount of preslip (Kame et al., 2014; Shreedharan et al., 2020), it is not unreasonable to expect some precursory signature in specific stiffness for natural faults undergoing a large increase in slip rate during preslip of a few cm. Additionally, dilatational and fluid pressure modulated mechanisms could enhance any existing precursory signatures in the preseismic stages (Scholz et al., 1973).

4.3. Variation in seismic velocities and attenuation: from the laboratory to nature

We explore the question of scaling and scalability of our experimental results to conditions relevant to nature in Fig. 7. A plot of relative variations in the raw (blue) and fault zone v_p (red) is shown in Fig. 7a for one laboratory stick-slip cycle. Variations are calculated relative to the v_p of the master waveform (star in Fig. 4c). The raw (combination of wallrock and fault zone) v_p primarily increases by ~0.1% during the interseismic period with a small precursory reduction of under 0.02% just prior to failure. In contrast, the fault zone v_p, primarily controlled by the preseismic acceleration on the fault, shows a significantly larger (~0.04%) precursor and the reduction in v_p occurs ~5 s before macroscopic frictional failure. We compare this to a recent study by Chiarabba et al. (2020) where they document velocity anomalies prior to the 30 October Mw 6.5 Norcia earthquake (Fig. 7b). Chiarabba et al. (2020) performed a time-lapse tomography of the fault structure using over 13000 nearby earthquakes over a period of three months to constrain the temporal evolution of regional v_p. Notably, relative to the background crustal v_p in the region (~6300 m/s), they observed a systematically increasing v_p signature (~5%) further away from the hypocenter (north node). Interestingly, they

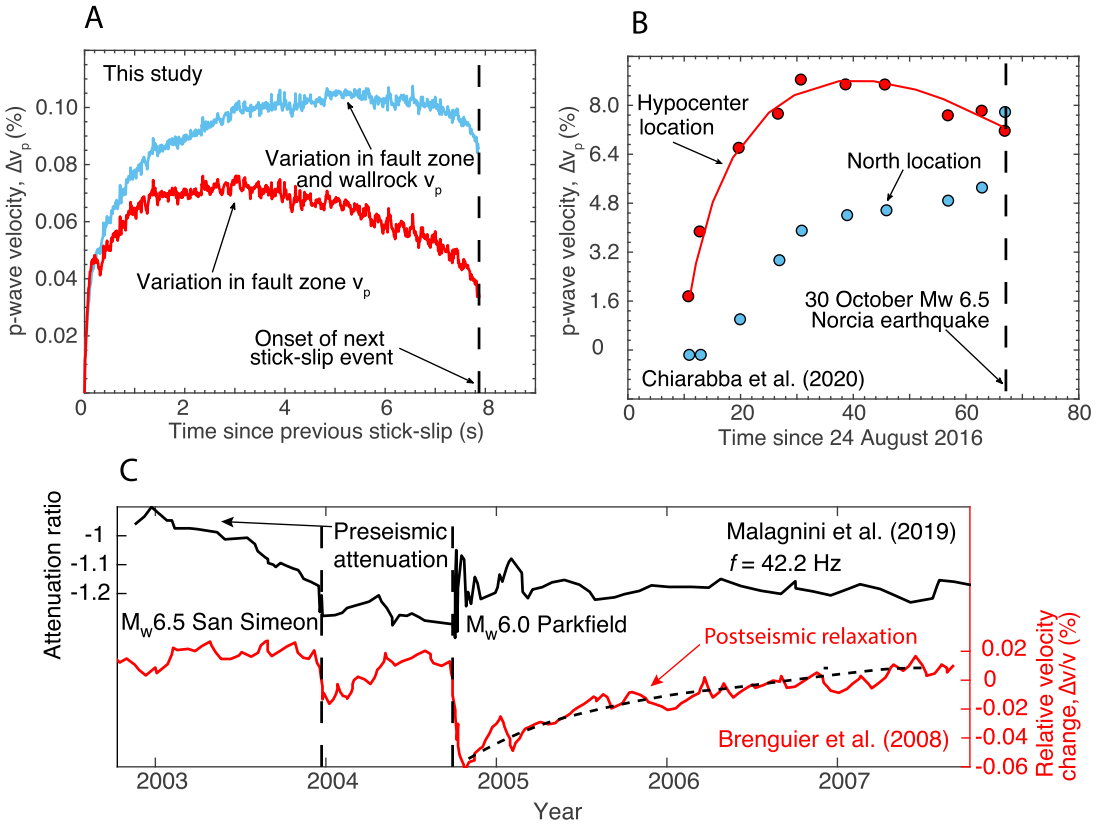

Fig. 7. Comparison between preseismic amplitude and velocity variations in our experiments and crustal systems (a) Relative variations in v_p during a seismic cycle (data from Fig. 4). Raw data (blue) encompassing the fault zone and wallrock shows a small and late preseismic v_p reduction whereas the fault zone v_p (red) has a larger and early onset precursory reduction. (b) Relative variations in v_p at the site of the Mw 6.5 Norcia earthquake. Data from a station close to the event (red) shows a precursory reduction in vp for ~25 days prior to the earthquake and data from a station further north (blue) shows a continuously increasing v_p trend. Modified from Chiarabba et al. (2020). (c) Time-series of P-wave velocity constrained from ambient noise cross-correlation (red) and seismic attenuation (black) for a 5 yr period from Oct 2002 – Sept 2007. Dashed vertical lines show the 2003 Mw 6.5 San Simeon and 2004 Mw 6.0 Parkfield earthquakes. Note the preseismic attenuation for ~10 months preceding the San Simeon earthquake and the postseismic relaxation of seismic velocities following the Parkfield earthquake, both of which are similar to the lab observations. Modified from Malagnini et al. (2019) and Brenguier et al. (2008).

also documented a precursory v_p reduction of ~3% at a node located near the Mw 6.5 earthquake hypocenter (red dots in Fig. 7b). They attribute these contrasting behaviors to a fault-wide elastic stiffening by tectonic loading causing a v_p increase and a precursory local (hypocentral) v_p reduction triggered by accelerated fault creep. This behavior is highly consistent with our experimental results. We note that our experimental v_p variations are approximately an order of magnitude smaller than those documented by Chiarabba et al. (2020). This could be due to fluid modulated processes (e.g. Saturation of pore spaces) further enhancing v_p variations in nature (Stanchits et al., 2003), which we do not consider in our experiments.

Previous experimental studies on the mechanics of frictional slip instabilities have used coda waves to document preseismic velocity variations of 0.5 – 1% and postseismic relaxations of up to 3% for coseismic stress drops of ~1 MPa (Fig. 4 in Kaproth and Marone, 2013; Fig. 4 in Scuderi et al., 2016). In our experiments (Fig. 4c), we document precursory velocity reductions of 0.02 – 0.04% and postseismic velocity recoveries of up to 0.1% of the nominal maximum P-wave (first-arrival) velocity. Ambient noise cross-correlation studies have documented post-seismic healing in the form of a logarithmic-with-time increase in seismic velocities of 0.02-0.06% after the 2003 M_w 6.5 San Simeon and the 2004 M_w 6.0 Parkfield earthquakes (Brenguier et al., 2008). Taken together, these results further demonstrate that existing field based time-lapse seismic studies have the necessary temporal resolution to constrain preseismic velocity/attenuation anomalies. Additionally, Malagnini et al. (2019) document robust seismic attenuation precursors at frequencies greater than 20 Hz for nearly 12 – 14 months prior to the 2003 M_w 6.5 San Simeon earthquake, and attribute this to variations in crack density in the fault damage zone (Fig. 7c). Interestingly, foreshock activity was only observed for a significantly shorter time interval (2-3 months) prior to this earthquake (Brenguier et al., 2008). Additionally, ambient noise cross-correlation studies (Brenguier et al., 2008) do not document any seismic velocity variation prior to this earthquake (Fig. 7c). Thus, we posit that in addition to variations in crack densities, preseismic increases in slip rate (and as a consequence, preseismic reduction in fault zone stiffness and contact area) may also be responsible for this preseismic attenuation. The absence of precursory velocity variations in ambient noise tomography studies could be because of a lower space-time resolution at seismogenic depths in these techniques or due to other mechanisms masking precursors (such as in our lab experiments).

In crustal faults, preseismic anomalies in attenuation and seismic velocities may depend on earthquake recurrence times, regional stress state, complexity of faulting, and importantly the amount of preseismic creep and its temporal duration. Given the temporal onset of resolvable precursors in our experiments, and in crustal studies (e.g. Niu et al., 2008; Malagnini et al., 2019; Chiarabba et al., 2020), it may not be unreasonable to expect near-field velocity anomalies on time scales of a few days to weeks, and attenuation anomalies for months prior to an earthquake. However, more field studies and data are necessary to validate this hypothesis. Regardless, existing field studies complement our experimental observations to show that seismic wave amplitude, in addition to

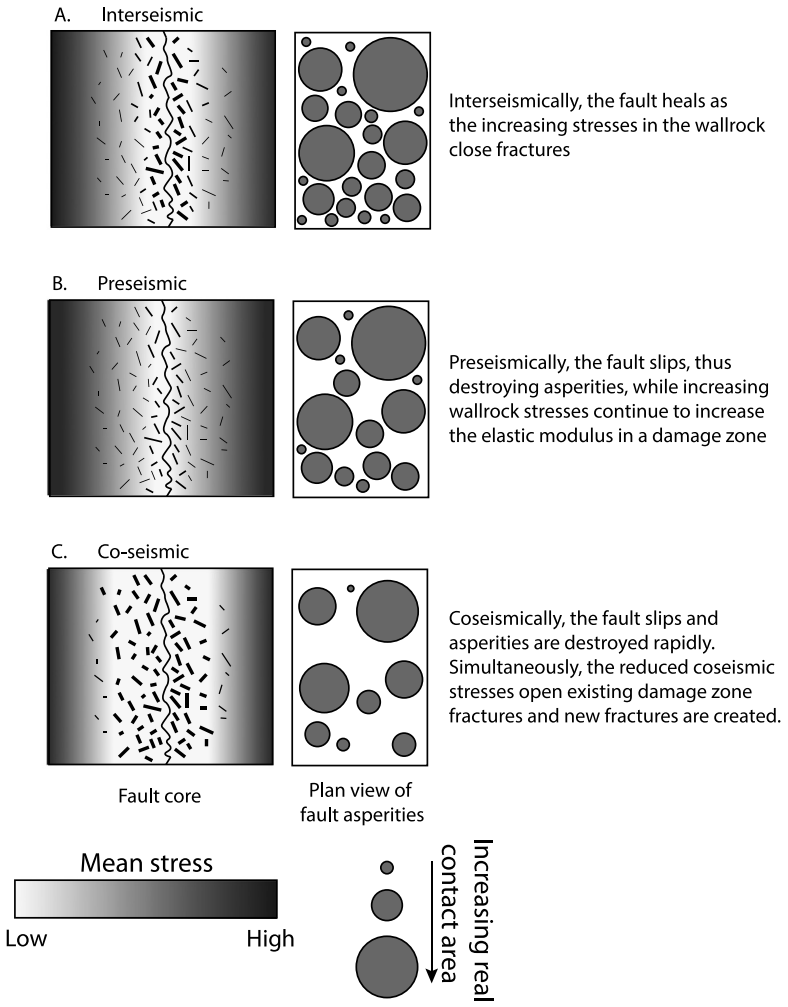

Fig. 8. Illustration of deformation mechanisms for fault zone and the surrounding damage zone. Left column shows the side-view of the fault and damage zone with lighter shades representing lower stresses in the wallrock. Closed fractures are shown as thinner black dashes and open fractures are represented by thicker dashes. Right hand column shows a plan view of the deforming asperities/micro-contacts in the fault zone. Larger asperities are represented by bigger circles. Illustrations are interpreted from the |T| and v_p variations documented in this study. Rows show the entire seismic cycle: (a) Interseismic (b) Preseismic and (c) Coseismic deformations (see Fig. 4A).

seismic velocity, may be a significant and highly sensitive probe to study transient crustal movements during the seismic cycle. A limited number of marine seismic surveys have demonstrated the feasibility of both spatial as well as temporal (e.g. Kodaira et al., 2012) observations of variations in reflected wave amplitudes at relevant depth/spatial resolutions and survey frequencies.

4.4. Physical mechanism for faults with damage zones

Here, we translate our experimental observations of |T| and v_p precursors into an illustrative physical mechanism for rough faults with a damage zone surrounding the fault core. We start with the interseismic phase (Fig. 8a) where the fault zone is healing and is also subjected to far field tectonic stressing due to plate motion. As the deviatoric stress in the damage zone increases, cracks will close locally and effective crack densities will reduce (Stanchits et al., 2003; Malagnini et al., 2019), increasing the effective elastic modulus of the wallrock. Simultaneously, the fault zone itself will undergo frictional healing and increased strength. Here, existing asperities increase in size and new contacts are created in an approximately logarithmic-with-time process (Shreedharan et al., 2019). These processes may manifest as an increase in seismic amplitudes and velocities. Fluid saturation and anisotropy will further modulate some of these effects (e.g. Hadley, 1976; Main, 1990; Stanchits et al., 2003).

The preseismic stage marks an increase in the rate of fault creep. In the context of tectonic faults, this would correspond to increased deviatoric stress in the damage zone as the fault begins to slip, thus destroying some of the asperities created in the interseismic (healing) stage. Our experiments provide direct evidence that a combination of these processes contributes to the precursory reduction of seismic wave amplitude and velocity. In our experiments, the amplitude signature is significantly more sensitive to preseismic deformation whereas the velocity variations are a product of trade-offs between fault creep and stressing. In nature, the magnitude and duration of precursory amplitude variations may scale with a combination of damage zone width, crack density, pore pressure, and damage zone dilation (Scholz et al., 1973; Dieterich, 1978; Brantut, 2015; Passelègue et al., 2016).

In the final, coseismic stage of the seismic cycle, the fault experiences a rapid increase in slip rate, destroying contact asperities, and the damage zone undergoes a reduction in deviatoric stress consistent with the seismic stress drop. This stress reduction will increase damage, open pre-existing fractures, and create new fractures. The destruction of asperities and increase in fracture density is expected to result in a coseismic reduction in |T| and v_p. We do not fully consider the effects of pore pressure, temperature and a mature damage zone on the evolution of precursory seismic attributes in the experimental results presented here and encourage future experimental research in these directions.

5. Conclusions

We report on the behavior of precursory variations in seismic amplitudes and velocities observed during laboratory earthquakes. Our results offer direct evidence for a long-term preseismic reduction in the amplitude of waves passing through the fault zone, consistent with existing models of preseismic fault creep. We also document a shorter-term preseismic velocity reduction and show that the duration of the velocity precursor is strongly affected by wallrock effects. We perform dynamic acoustoelastic testing (DAET) experiments to isolate the impact of processes within the wallrock and those within the fault zone on seismic wave attenuation and velocity. Our results indicate that seismic amplitudes are more sensitive to changes in the fault zone whereas wave speed is affected by both the wallrock stress state and fault zone processes. We recast the |T| and velocity observations into an equivalent fault zone contact stiffness and document systematic precursory variations in contact stiffness before stick-slip failure.

The relative variations in our precursory amplitude and velocity signatures are also consistent with pre- co- and post-seismic P-wave attenuation and velocities observed in meso- and macroscopic dynamic systems in nature. These complementary observations offer some context for scaling our results to natural faults. Although we do not consider the effect of pore fluid pressure, temperature and dilatational, all of these effects could impact our observations of preseismic amplitude and velocity variations and should be addressed in future research. Our work provides laboratory evidence for the utility of active seismic monitoring of crustal faults for hazard mitigation, and a physical basis for the interpretation of seismic amplitude and velocity variations during the seismic cycle.

CRediT authorship contribution statement

Srisharan Shreedharan: Conceptualization, Methodology, Investigation, Writing – Original Draft, Funding Acquisition

David Chas Bolton: Methodology, Investigation, Writing – Review and Editing

Jacques Rivière: Methodology, Software, Investigation, Writing – Review and Editing

Chris Marone: Conceptualization, Methodology, Investigation, Writing – Review and Editing, Supervision, Funding Acquisition

Declaration of competing interest

The authors declare that they have no known competing financial interests or personal relationships that could have appeared to influence the work reported in this paper.

Acknowledgements

Much of this manuscript was inspired by a conversation with Allan Rubin at the Gordon Research Conference for Rock Deformation 2018. We thank Demian Saffer and Charles Ammon for their input. We thank Rebecca Bendick, Claudio Chiarabba and three anonymous reviewers for their comments which helped improve the manuscript. Technical assistance from Steven Swavely and further input from Josie Marone is gratefully acknowledged. This study was supported by European Research Council Advance Grant 835012 (TECTONIC), US Department of Energy grants DE-SC0020512 and DE-EE0008763, and US National Science Foundation grants EAR – 1520760 and EAR – 1547441 to C.M., and an International Ocean Discovery Program (IODP) Schlanger Ocean Drilling Fellowship to S.S. Data is available from the PSU Scholarsphere repository or by contacting the corresponding author.

Appendix A. Supplementary material

Supplementary material related to this article can be found online at https://doi.org/10.1016/j.epsl.2020.116623.

References

Aben, F.M., Brantut, N., Mitchell, T.M., David, E.C., 2019. Rupture energetics in crustal rock from laboratory-scale seismic tomography. Geophys. Res. Lett. 46 (13), 7337–7344.

Acosta, M., Passelègue, F.X., Schubnel, A., Madariaga, R., Violay, M., 2019. Can precursory moment release scale with earthquake magnitude? A view from the laboratory. Geophys. Res. Lett. 46 (22), 12927–12937.

Adams, L.H., Williamson, E.D., 1923. On the compressibility of minerals and rocks at high pressures. J. Franklin Inst. 195 (4), 475–529.

Amoruso, A., Crescentini, L., 2012. Pre-seismic phenomena from continuous near-field strain measurements: a brief review and the case of the 2009 L'Aquila, Italy, earthquake. Boll. Geofis. Teor. Appl. 53 (1).

Bakun, W.H., Aagaard, B., Dost, B., Ellsworth, W.L., Hardebeck, J.L., Harris, R.A., Ji, C., Johnston, M.J.S., Langbein, J., Lienkaemper, J.J., Michael, A.J., 2005. Implications for prediction and hazard assessment from the 2004 Parkfield earthquake. Nature 437 (7061), 969–974.

Brace, W.F., Paulding, B.W., Scholz, C., 1966. Dilatancy in the fracture of crystalline rocks. J. Geophys. Res. 71 (16), 3939–3953. https://doi.org/10.1029/JZ071i016p03939.

Brantut, N., 2015. Time-dependent recovery of microcrack damage and seismic wave speeds in deformed limestone. J. Geophys. Res., Solid Earth 120 (12), 8088–8109.

Brenguier, F., Campillo, M., Hadziioannou, C., Shapiro, N.M., Nadeau, R.M., Larose, E., 2008. Postseismic relaxation along the San Andreas fault at Parkfield from continuous seismological observations. Science 321 (5895), 1478–1481.

Céspedes, I., Huang, Y., Ophir, J., Spratt, S., 1995. Methods for estimation of subsample time delays of digitized echo signals. Ultrason. Imag. 17 (2), 142–171.

Chiarabba, C., De Gori, P., Segou, M., Cattaneo, M., 2020. Seismic velocity precursors to the 2016 Mw 6.5 Norcia (Italy) earthquake. Geology.

Cicerone, R.D., Ebel, J.E., Britton, J., 2009. A systematic compilation of earthquake precursors. Tectonophysics 476 (3–4), 371–396.

Dieterich, J.H., 1978. Preseismic fault slip and earthquake prediction. J. Geophys. Res., Solid Earth 83 (B8), 3940–3948.

Frye, K.M., Marone, C., 2002. The effect of particle dimensionality on granular friction in laboratory shear zones. Geophys. Res. Lett. 29 (19), 1916. https://doi.org/10.1029/2002GL015709.

Geller, R.J., 1997. Earthquake prediction: a critical review. Geophys. J. Int. 131 (3), 425–450.

Hadley, K., 1976. Comparison of calculated and observed crack densities and seismic velocities in Westerly granite. J. Geophys. Res. 81 (20), 3484–3494.

Hedayat, A., Pyrak-Nolte, L.J., Bobet, A., 2014. Precursors to the shear failure of rock discontinuities. Geophys. Res. Lett. 41 (15), 5467–5475.

Hedayat, A., Haeri, H., Hinton, J., Masoumi, H., Spagnoli, G., 2018. Geophysical signatures of shear-induced damage and frictional processes on rock joints. J. Geophys. Res., Solid Earth 123 (2), 1143–1160.

Kame, N., Nagata, K., Nakatani, M., Kusakabe, T., 2014. Feasibility of acoustic monitoring of strength drop precursory to earthquake occurrence. Earth Planets Space 66 (1), 41.

Kaproth, B.M., Marone, C., 2013. Slow earthquakes, preseismic velocity changes, and the origin of slow frictional stick-slip. Science 341 (6151), 1229–1232.

Kendall, K., Tabor, D., 1971. An utrasonic study of the area of contact between stationary and sliding surfaces. Proc. R. Soc. Lond. Ser. A, Math. Phys. Sci. 323 (1554), 321–340.

Kenigsberg, A.R., Rivière, J., Marone, C., Saffer, D.M., 2019. The effects of shear strain, fabric, and porosity evolution on elastic and mechanical properties of clay-rich fault gouge. J. Geophys. Res., Solid Earth 124 (11), 10968–10982.

Kilgore, B., Beeler, N.M., Lozos, J., Oglesby, D., 2017. Rock friction under variable normal stress. J. Geophys. Res., Solid Earth 122 (9), 7042–7075.

Kodaira, S., No, T., Nakamura, Y., Fujiwara, T., Kaiho, Y., Miura, S., Takahashi, N., Kaneda, Y., Taira, A., 2012. Coseismic fault rupture at the trench axis during the 2011 Tohoku-oki earthquake. Nat. Geosci. 5 (9), 646–650.

Knuth, M.W., Tobin, H.J., Marone, C., 2013. Evolution of ultrasonic velocity and dynamic elastic moduli with shear strain in granular layers. Granul. Matter 15 (5), 499–515.

Leeman, J.R., Saffer, D.M., Scuderi, M.M., Marone, C., 2016. Laboratory observations of slow earthquakes and the spectrum of tectonic fault slip modes. Nat. Commun. 7 (1), 1–6.

Main, I.G., 1990. Quasi-static modelling of stress histories during the earthquake cycle: precursory seismic and aseismic stress release. Geophys. J. Int. 102 (1), 195–203.

Main, I.G., Bell, A.F., Meredith, P.G., Geiger, S., Touati, S., 2012. The dilatancy–diffusion hypothesis and earthquake predictability. Geol. Soc. (Lond.) Spec. Publ. 367 (1), 215–230.

Malagnini, L., Dreger, D.S., Bürgmann, R., Munafò, I., Sebastiani, G., 2019. Modulation of seismic attenuation at Parkfield, before and after the 2004 M6 earthquake. J. Geophys. Res., Solid Earth 124 (6), 5836–5853.

Melbourne, T.I., Webb, F.H., 2002. Precursory transient slip during the 2001 M_w= 8.4 Peru earthquake sequence from continuous GPS. Geophys. Res. Lett. 29 (21), 2032. https://doi.org/10.1029/2002GL015533.

Milne, J., 1880. Seismic science in Japan. Transact. Seismol. Soc. Japan 1, 3–34.

Nagata, K., Nakatani, M., Yoshida, S., 2008. Monitoring frictional strength with acoustic wave transmission. Geophys. Res. Lett. 35 (6).

Niu, F., Silver, P.G., Daley, T.M., Cheng, X., Majer, E.L., 2008. Preseismic velocity changes observed from active source monitoring at the Parkfield SAFOD drill site. Nature 454 (7201), 204–208.

Stanchits, S.A., Lockner, D.A., Ponomarev, A.V., 2003. Anisotropic changes in P-wave velocity and attenuation during deformation and fluid infiltration of granite. Bull. Seismol. Soc. Am. 93 (4), 1803–1822.

Passelègue, F.X., Spagnuolo, E., Violay, M., Nielsen, S., Di Toro, G., Schubnel, A., 2016. Frictional evolution, acoustic emissions activity, and off-fault damage in simulated faults sheared at seismic slip rates. J. Geophys. Res., Solid Earth 121 (10), 7490–7513.

Passelègue, F.X., Latour, S., Schubnel, A., Nielsen, S., Bhat, H.S., Madariaga, R., 2017. Influence of fault strength on precursory processes during laboratory earthquakes. In: Fault Zone Dynamic Processes: Evolution of Fault Properties During Seismic Rupture, vol. 227, p. 229.

Paterson, M.S., Wong, T.F., 2005. Experimental Rock Deformation - The Brittle Field. Springer Science & Business Media.

Pei, S., Niu, F., Ben-Zion, Y., Sun, Q., Liu, Y., Xue, X., Su, J., Shao, Z., 2019. Seismic velocity reduction and accelerated recovery due to earthquakes on the Longmenshan fault. Nat. Geosci. 12 (5), 387–392.

Pritchard, M.E., Allen, R.M., Becker, T.W., Behn, M.D., Brodsky, E.E., Bürgmann, R., Ebinger, C., Freymueller, J.T., Gerstenberger, M., Haines, B., Kaneko, Y., 2020. New opportunities to study earthquake precursors. Seismol. Res. Lett.

Pyrak-Nolte, L.J., Myer, L.R., Cook, N.G., 1990. Transmission of seismic waves across single natural fractures. J. Geophys. Res., Solid Earth 95 (B6), 8617–8638.

Rivière, J., Renaud, G., Guyer, R.A., Johnson, P.A., 2013. Pump and probe waves in dynamic acousto-elasticity: comprehensive description and comparison with nonlinear elastic theories. J. Appl. Phys. 114 (5), 054905.

Rivière, J., Pimienta, L., Scuderi, M., Candela, T., Shokouhi, P., Fortin, J., Schubnel, A., Marone, C., Johnson, P.A., 2016. Frequency, pressure, and strain dependence of nonlinear elasticity in Berea Sandstone. Geophys. Res. Lett. 43. https://doi.org/10.1002/2016GL068061.

Sammonds, P.R., Meredith, P.G., Main, I.G., 1992. Role of pore fluids in the generation of seismic precursors to shear fracture. Nature 359 (6392), 228–230.

Savage, H.M., Brodsky, E.E., 2011. Collateral damage: evolution with displacement of fracture distribution and secondary fault strands in fault damage zones. J. Geophys. Res., Solid Earth 116 (B3).

Scholz, C.H., Sykes, L.R., Aggarwal, Y.P., 1973. Earthquake prediction: a physical basis. Science 181 (4102), 803–810.

Scuderi, M.M., Marone, C., Tinti, E., Di Stefano, G., Collettini, C., 2016. Precursory changes in seismic velocity for the spectrum of earthquake failure modes. Nat. Geosci. 9 (9), 695–700.

Scuderi, M.M., Collettini, C., Viti, C., Tinti, E., Marone, C., 2017. Evolution of shear fabric in granular fault gouge from stable sliding to stick slip and implications for fault slip mode. Geology 45 (8), 731–734.

Shimazaki, K., Nakata, T., 1980. Time-predictable recurrence model for large earthquakes. Geophys. Res. Lett. 7 (4), 279–282.

Shreedharan, S., Rivière, J., Bhattacharya, P., Marone, C., 2019. Frictional state evolution during normal stress perturbations probed with ultrasonic waves. J. Geophys. Res., Solid Earth 124 (6), 5469–5491.

Shreedharan, S., Bolton, D.C., Rivière, J., Marone, C., 2020. Preseismic fault creep and elastic wave amplitude precursors scale with lab earthquake magnitude for the continuum of tectonic failure modes. Geophys. Res. Lett., e2020GL086986.

Uchida, N., Matsuzawa, T., 2013. Pre- and postseismic slow slip surrounding the 2011 Tohoku-oki earthquake rupture. Earth Planet. Sci. Lett. 374, 81–91.